JOURNAL OF GEOPHYSICAL RESEARCH, VOL. 105, NO. B9, PAGES 21,543–21,557, SEPTEMBER 10, 2000

Shear wave speeds at the base of the mantle

John C. Castle[1]

Department of Earth, Atmospheric, and Planetary Sciences, Massachusetts Institute of Technology, Cambridge

Kenneth C. Creager and John P. Winchester

Geophysics Program, University of Washington, Seattle

Rob D. van der Hilst

Department of Earth, Atmospheric, and Planetary Sciences, Massachusetts Institute of Technology, Cambridge

Abstract. We inverted 4864 *ScS-S* and 1671 S_{diff}-*SKS* residual travel times for shear wave speed anomalies at the base of the Earth's mantle. We applied ellipticity corrections, accounted for mantle structure outside of the basal layer using mantle tomography models, and used finite size sensitivity kernels. The basal layer thickness was set to 290 km; however, the data allow thicknesses between 200 and 500 km. The residuals were inverted using a spherical harmonic basis set of degree 30 for a model that both is smooth and has a small Euclidean norm, which limited spectral leakage of higher-order structures into low-order wavelengths. Hotspots dominantly overlay slow wave speed regions. Nonsightings of ultralow-velocity zones (ULVZs) most frequently appear in fast regions, suggesting that slow regions at the base of the mantle are associated with ULVZs. However, ULVZ sightings appear in both slow and fast regions. Recently active subduction zones do not correlate with velocity anomalies; however, the locations of subduction zones active prior to 90 Ma correlate extremely well with fast anomalies, implying that slabs descend as fast as 2 cm yr^{-1} through the lower mantle. The correlation continues through the historical subduction record to 180 Ma, suggesting that slabs remain in the deep mantle at least 90 Myr. Fast anomalies reach +2%, while slow anomalies extend to -5%. If we assume that the anomalies are thermal and anharmonic in origin and apply a wave speed/thermal anomaly conversion, the temperature deviations would be over -500°K (cold) in fastest regions and over +1000°K (hot) in the slowest regions, which would initiate plumes much hotter than those observed at the surface. Alternative explanations for the large anomalies are widespread partial melt or compositional differences in the lowermost mantle.

1. Introduction

The core-mantle boundary (CMB) is a thermal and compositional boundary where wave speeds and electrical properties are discontinuous [*Liu*, 1979]. Localized regions of partial melt may exist in the lowest 10-50 km of the mantle [e.g., *Garnero et al.*, 1998]. Horizontal thermal and electrical anomalies may couple the outer core flow field to the mantle [e.g., *Bloxham and Gubbins*, 1987], and density anomalies may couple the mantle to the inner core [*Buffett*, 1997]. *S* and *P* wave travel time curves exhibit a change in slope in the lower 150 km of the mantle; this region was labeled D" in the original classification nomenclature of *Bullen* [1955]. *S* and *P* waves sampling the lowermost 300 km of the mantle have revealed structures not predicted by global models, such as sharp gradients in wave speeds (see *Wysession* [1996a] and *Wysession et al.* [1998] for recent summaries).

Key to unraveling these interactions are observations of the lowermost mantle. For instance, early seismic tomographic images show that a degree 2 pattern characterizes the dominant D" wave speed structure well, with slow shear wave propagation beneath Africa and the central Pacific surrounded by fast regions around the edges of the Pacific Ocean. That this pattern correlates well with historical subduction in the past 150 Myr suggests that some slabs reach the lower mantle [*Su and Dziewonski*, 1991; *Richards and Engebretson*, 1992].

This study presents the results of a tomographic inversion of *ScS-S* and S_{diff}(diffracted *S*)-*SKS* travel time residuals for horizontal structure at the base of the mantle. We first took into account three-dimensional (3-D) whole mantle structure outside of the basal layer. By inverting for a 2-D model at the base of the mantle, rather than for a more complete 3-

[1] Previously at Geophysics Program, University of Washington, Seattle.

Paper number 2000JB900193.
0148-0227/00/2000JB900193$09.00

D whole mantle model, we reduced the computational resources necessary for a single inversion such that we could efficiently run many inversions to estimate error bounds, test the effect of sensitivity kernels, and test the influence of different damping (regularization) parameters. We find that fast anomalies correlate well to older subduction zones (>90 Ma), hotspot locations correlate well to slow anomalies, recently discovered ultralow-velocity zones (ULVZs) at the base of the mantle exist in both slow and fast wave speed regions, and the magnitude of the anomalies in our model cannot be purely explained in terms of thermal structure.

Where we do not state otherwise, we inverted the data using a basal layer thickness of 290 km. We also inverted the data using different basal layer thicknesses and found that the travel time data can be satisfied by layers between 190 and 490 km thick (but not thicker). Thus while both the *ScS-S* and S_{diff}-*SKS* residual times are most sensitive to structure at the base of the mantle, they cannot be assumed to image only a limited basal layer (i.e., D" or a 300-km-thick layer) but should be considered a vertical average of the base of the mantle.

2. *ScS-S* and S_{diff}-*SKS* Travel Times

We determined shear wave propagation speeds in the deep mantle using *ScS-S* and S_{diff}-*SKS* travel time residuals. Figure 1 shows the *ScS*, S_{diff}, and *SKS* ray paths through the mantle. We accounted for travel time contributions from structures outside of the basal layer and inverted the remaining travel time residuals for velocity anomalies in the basal layer.

The differential residual times of these two phase pairs are particularly useful for determining velocities in the lowermost mantle [*Valenzuela and Wysession*, 1998]. First, both phases in each pair similarly sample near-source structure. Thus errors due to earthquake mislocation and local velocity structures are reduced. Second, the *ScS* and S_{diff} phases have long path lengths in the basal layer. Finally, by combining the two data sets, we achieved near global coverage and expanded on the previous studies of *Woodward and Masters* [1991], *Garnero and Helmberger* [1993], *Wysession et al.* [1994], *Sylvander and Souriau* [1996], and *Kuo and Wu* [1997].

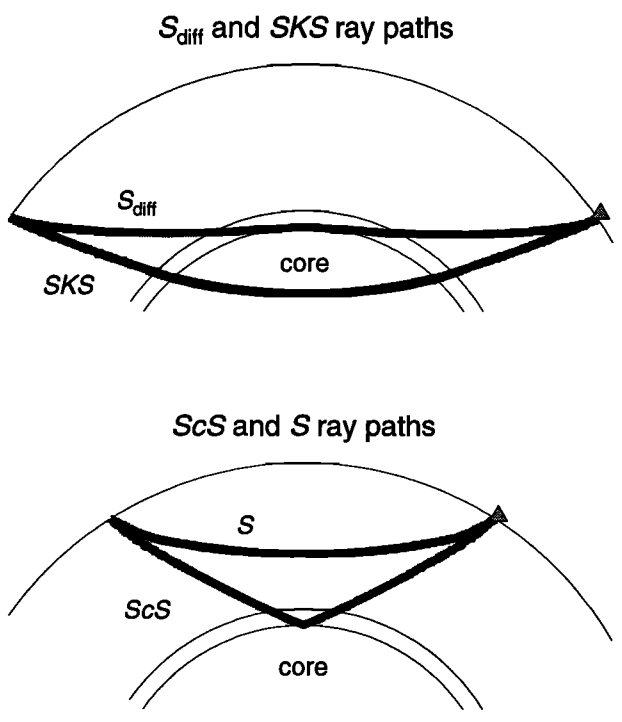

Figure 1. Ray paths for (top) S_{diff}-*SKS* and (bottom) *ScS-S*.

2.1. S_{diff}-*SKS* Travel Times

We collected the S_{diff}-*SKS* travel time data from data sets previously picked by B. Kuo (733 points) [*Kuo and Wu*, 1997] and E. Garnero (1624 points) [*Garnero and Helmberger*, 1993; B. Y. Kuo et al.,Tomographic inversion of *S-SKS* times for shear velocity heterogeneity in D": Degree 12 and hybrid models, submitted to Journal of Geophysical Research, 2000, hereinafter referred to as Kuo et al., submitted manuscript, 2000]. The Kuo data have good global coverage, including extensive Southern Hemisphere coverage, while the Garnero data have excellent circum-Pacific coverage.

The Kuo data were assembled from the Geoscope network, the Global Seismic Network (GSN), and the Global Digital Seismic Network (GDSN). All of the data were filtered to a long-period GDSN station instrument response, which peaks at 30 s periods, and they were rotated into radial and transverse components. The residual times were picked by correlating the largest waveform swing of the *SKS* arrival on the radial component to the corresponding swing of the S_{diff} arrival on the transverse component. The picks were checked by correlating waveforms generated by reflectivity seismograms.

The Garnero data set included *S* and *SKS* readings from digital networks from 1993 to 1997, including GSN, United States National Seismic Network (USNSN), Canadian National Seismic Network (CNSN), World Wide Standardized Seismograph Network (WWSSN), Incorporated Research Institutes for Seismology (IRIS), and Program for Array Seismic Studies of the Continental Lithosphere (PASSCAL) data [*Young and Lay*, 1990; *Garnero and Helmberger*, 1993; Kuo et al., submitted manuscript, 2000]. These data also comprised readings from digitized analog WWSSN records with a frequency response peaked near 20 s periods. The S_{diff} and *SKS* arrival times were picked by hand to reduce possible errors from the variable shape of S_{diff}.

Garnero's data included *S-SKS* data in which the *S* leg does not diffract. We used the subset of his data for which the S_{diff} leg through the basal layer is at least twice as long as the sum of the two *SKS* legs. This corresponds to a minimum epicentral distance of about 90°. This restriction eliminated 530 travel times.

Furthermore, we used the hypocenters of *Engdahl et al.* [1998] in our processing and eliminated data for which no hypocenter existed in this catalog (330 travel times). We ended with 473 data points from the Kuo data set and 1198 points from the Garnero data set.

2.2. *ScS-S* Travel Times

We also used 3492 *ScS-S* times picked by *Masters et al.* [1996] and 1372 *ScS-S* and *sScS-sS* of our own picks [*Winchester and Creager*, 1997]. Both data sets were compiled from the GDSN, the GSN, and the Geoscope networks, and *Masters et al.* [1996] and *Winchester and Creager* [1997] calculated travel times using similar cross-correlation methods [*Woodward and Masters*, 1991].

Winchester and Creager [1997] band-pass-filtered displacement seismograms from 8 to 60 s. As attenuation changes waveform shapes, especially the latter parts of waveforms [*Woodward and Masters*, 1991], they incorporated it by convolving each *ScS* waveform with a Futterman filter using a differential (*ScS-S*) t^* operator calculated using the shear wave attenuation (Q_s^{-1}) from the Preliminary Reference Earth model (PREM) [*Dziewonski and Anderson*, 1981]. The relative arrival time of *ScS* to *S* was picked by cross-correlating the first swing of each waveform, which favors the higher-frequency part of the waveform.

Masters et al. [1996] filtered data to the Abbreviated Seismic Research Observatory (ASRO) long-period response, peaked near 20 s periods, and picked differential times using a cross-correlation method that weighted the early part of the arrivals higher than the later parts. Among the 230 redundant picks between the Masters and Winchester data sets, the root-mean-square (rms) difference in differential travel time is <1 s.

To avoid complications from the upper mantle transition zone discontinuities, we chose data with epicentral distances >30° for the *ScS-S* and >45° for the *sScS-sS*. To avoid misidentification of the *ScS* and *S* phases, the epicentral distances were limited to under 80°. Finally, the *sScS-sS* data were selected only from earthquakes at depths >100 km such that there was clear separation between the surface reflected and direct phases.

2.3. Data Coverage

Figure 2 shows the coverage for the data sets. The *ScS-S* data set (Figure 2c) has extensive coverage beneath eastern Asia, Australia, Alaska, and Central America. However, the *ScS-S* data lack coverage in the central and south central Pacific. The S_{diff}-*SKS* (Figure 2a) data set provides excellent complementary coverage with extensive coverage beneath the central Pacific Ocean in addition to more Southern Hemisphere data. Where the data sets overlap, such as under the northwest Pacific, the Philippines, and Africa, the agreement of the sign and magnitude of the anomalies is impressive (Figures 2b and 2d).

3. Inversion

We calculated differential travel time residuals for the phase pairs *ScS-S*, *sScS-sS*, and S_{diff}-*SKS* by subtracting the

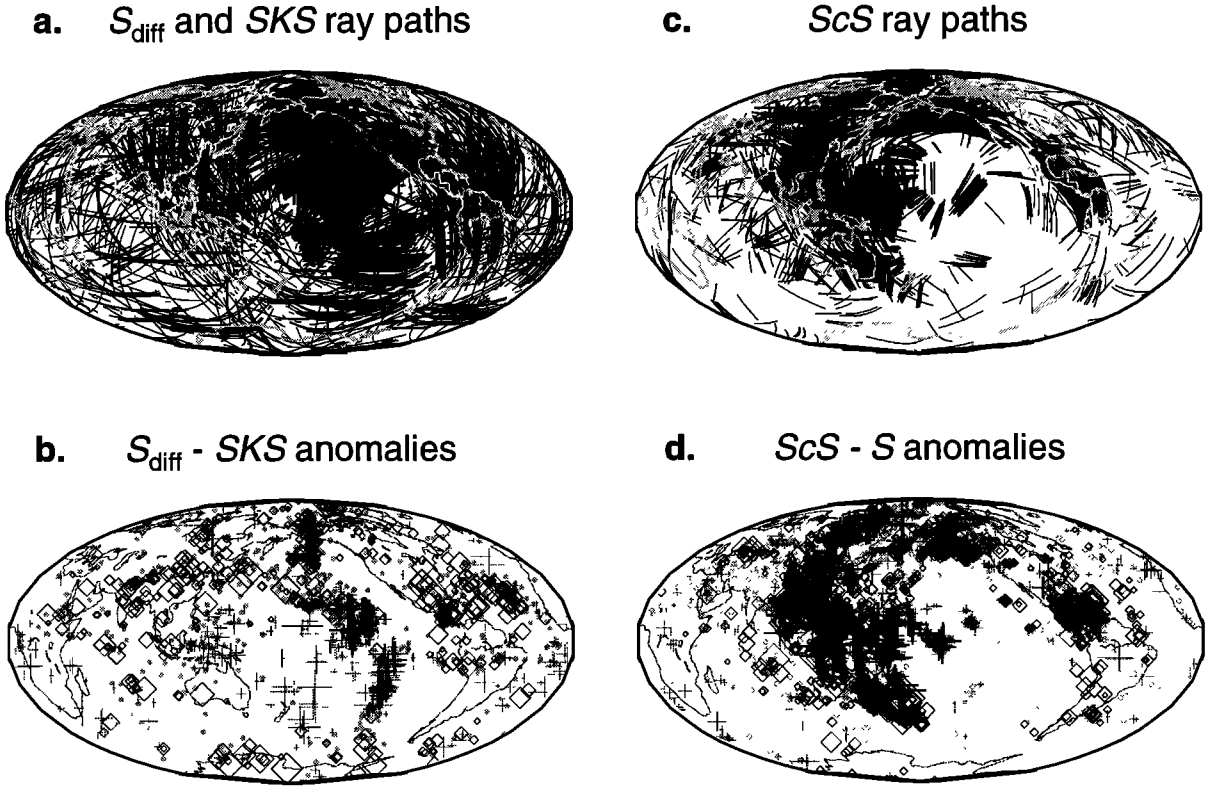

Figure 2. Ray paths in the basal layer for: (a) S_{diff} and *SKS*, and (c) *ScS*. (b and d) Travel time anomalies, scaled by the travel time in the basal layer, at the midpoint of the S_{diff} and *ScS* ray paths. Crosses mark slow velocities, circles mark values within one-half standard deviation of zero, and diamonds mark fast anomalies. Symbol size is proportional to scaled anomaly magnitude.

predicted travel time difference from the observed differential times. We calculated predicted times for each pair using ray theory, earthquake hypocenters estimated by *Engdahl et al.* [1998], the isotropic PREM model [*Dziewonski and Anderson*, 1981], and corrections for the Earth's ellipticity [*Dziewonski and Gilbert*, 1976]. We also used several global tomography models to correct for mantle structure above the region of our current interest.

Most previous basal mantle studies used the PREM model; in order to easily compare models we also used PREM. However, the hypocenters of *Engdahl et al.* [1998] were determined in the model ak135 [*Kennett et al.*, 1995]. Using the PREM model and hypocenters determined in the ak135 model may introduce an error, but in the context of the differential residual times, this error is insignificant. The predicted S_{diff}-*SKS* residual travel times from PREM are roughly 0.8 s smaller than predicted from ak135 over the distance range 90° to 130°, largely due to V_p differences at the top of the outer core. This uncertainty is small compared to the observed S_{diff}-*SKS* residual travel times, which range from -20 to +20 s.

3.1. Inversion Method

To invert the observed travel time residuals for velocity structure, we define the forward problem

$$\mathbf{A}\underline{\mathbf{m}} = \underline{\mathbf{d}}, \tag{1}$$

where $\underline{\mathbf{m}}$ is the vector containing $M = (L+1)^2$ spherical harmonic model coefficients, $\underline{\mathbf{d}}$ is the vector of N observed differential travel time residuals, and $\mathbf{A}$ is the matrix of the sensitivity of each travel time residual to model coefficients, size $N \times M$. The model is shear wave velocity anomaly divided by the shear wave velocity of PREM.

3.1.1. The A matrix. $\mathbf{A}$ represents the functional dependence of the travel time residuals on individual spherical harmonic coefficients. Because the travel times were measured at comparatively low frequencies (10-30 s period), we did not assume infinite frequency ray paths but instead calculated two-dimensional sensitivity kernels for the rays within the basal layer. While infinite frequency rays are sensitive to structure along a narrow ray path, the waveform of a finite frequency arrival is sensitive to a broader region around the ray path; the dependence of a waveform on mantle structure is called a Fréchet or sensitivity kernel [*Zhao et al.*, 2000].

Here we simply designed the kernels by calculating the Fresnel volume (half period) at the dominant period for each observation using a Kirchoff method (Figure 3). The first Fresnel volume is defined as the locus of points where the travel time from the source to that point plus the travel time from that point to the receiver minus the direct source to receiver travel time is less than half the period of the observed wave. We approximated the Fresnel zone by an ellipse [*Wysession*, 1996b]. The kernels decay away from the ray path as described by a Gaussian function which decays to $(2e)^{-1}$ of its maximum value at the first Fresnel Zone. These finite volume sensitivity kernels efficiently approximate the formal Fréchet kernels of *Zhao et al.* [2000]. We note, however, that our 2-D approximated sensitivity ellipses would not be useful for approximating 3-D kernels of multiply reflected phases such *SS* [*Neele et al.*, 1997; *Zhao et al.*, 2000]. We normalized each kernel so that its integral over the basal layer equaled the distance the ray travels in the basal layer; thus, in the limiting case of narrow Fresnel volumes (high frequency) we obtain the same sensitivity as ray theory. Figure 3 shows the *SKS* and S_{diff} Fresnel zones for a surface earthquake recorded at 103.5° and at 30 s period. The forward problem defined in equation (1) is identical to the integral over the unit sphere of an inner product of the Fréchet kernels and the model. With this formulation the power of inverse theory [e.g., *Parker*, 1994] can be used.

The ith row of the $\mathbf{A}$ matrix contains the coefficients of a spherical harmonic expansion of the differential kernels for the ith observed times. An efficient algorithm to compute these coefficients is to evaluate and store each spherical harmonic basis function on a latitude, longitude grid. We used 2.5° grid spacing. Each kernel is evaluated on this grid, and each element of $\mathbf{A}$ is the integral over this grid of a kernel and a spherical harmonic.

To generate the $\mathbf{A}$ matrix, we repeated this procedure for both the *ScS-S* and S_{diff}-*SKS* data sets. For the S_{diff}-*SKS* kernels we included contributions from both the S_{diff} path and the *SKS* paths through the basal layer. Because basal layer velocity anomalies along the *SKS* path affect S_{diff}-*SKS* residual time opposite to anomalies along the S_{diff} path, the *SKS* kernels were subtracted from $\mathbf{A}$.

3.1.2. Inversion. We expanded shear wave velocity perturbations, with respect to PREM, in the basal layer as

$$\delta V(\theta,\phi) = \sum_{l=0}^{30}\sum_{m=0}^{l}(a_l^m \cos m\phi + b_l^m \sin m\phi)\mathrm{P}_l^m(\cos\theta) \tag{2}$$

using the associated Legendre polynomial scaling of *Merrill et al.* [1998]. The model parameters (a_l^m, b_l^m) are stored in the vector $\underline{\mathbf{m}}$. For each l, there are $2l+1$ parameters because b_l^0 is not needed.

Following the nomenclature of *Parker* [1994], we defined the square of the "size" of the model as

$$S_0^2 = \frac{1}{4\pi}\int_0^{2\pi}\int_0^{\pi}(\delta V)^2 \sin\theta d\theta d\phi = \sum_{l=0}^{30}\sum_{m=0}^{l}(a_l^m)^2 + (b_l^m)^2 \tag{3}$$

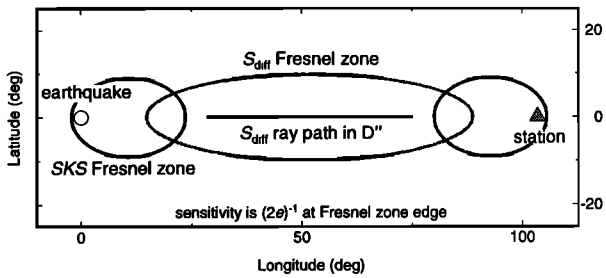

Figure 3. The Fresnel zones for the S_{diff} leg and *SKS* legs in the 290 km above the CMB from a surface earthquake recorded at 103.5° at 30 s periods. See also Plate 1.

and the square of the "roughness" by the integral over the basal layer of the squares of the surface Laplacian:

$$S_2^2 = \frac{1}{4\pi}\int_0^{2\pi}\int_0^{\pi}(\nabla_S^2\delta V)^2 \sin\theta d\theta d\phi = \sum_{l=0}^{30}\sum_{m=0}^{l} l^2(l+1)^2[(a_l^m)^2 + (b_l^m)^2]. \quad (4)$$

We sought a solution that is simultaneously "smallest" (minimizing S_0 and closest to PREM) and "smoothest" (minimizing S_2) and provides an adequate fit to the data. Data misfit is measured in a least squares sense as

$$\mathrm{M} = (\underline{\mathbf{d}} - \mathbf{A}\underline{\mathbf{m}} - \underline{\mathbf{p}})^{\mathrm{T}}(\underline{\mathbf{d}} - \mathbf{A}\underline{\mathbf{m}} - \underline{\mathbf{p}}), \quad (5)$$

where $\underline{\mathbf{p}}$ is the vector containing the travel time corrections from 3-D models outside of the basal layer and $\mathbf{A}\underline{\mathbf{m}}$ is the vector of travel time predictions from the basal layer. Variance reduction is defined as

$$\text{variance reduction} = 1 - \frac{\mathrm{M}}{\underline{\mathbf{d}}^{\mathrm{T}}\underline{\mathbf{d}}}100\%. \quad (6)$$

A solution that simultaneously minimizes data misfit, model size, and model roughness requires two trade-off parameters, β and L_o. We found solutions that minimize

$$\mathrm{M} + \beta[L_0^2(L_0^2+1)S_0 + S_2].$$

For a given β and L_o the model parameters that minimize the above expression were

$$\underline{\mathbf{m}} = (\mathbf{A}^{\mathrm{T}}\mathbf{A} + \mathbf{D})^{-1}\mathbf{A}^{\mathrm{T}}\underline{\mathbf{d}} \quad (7)$$

where $\mathbf{D}$ is a diagonal regularization matrix with elements defined by

$$\mathbf{D}(i,i) = \beta \times L_0^2(L_0+1)^2\left[1 + \frac{l(i)^2(l(i)+1)^2}{L_0^2(L_0+1)^2}\right](\text{nosum}) \quad (8)$$

where i runs from 1 to M; $l(i)$ is the order of the Legendre polynomial at that index: $l(1) = 0, l(2,3,4) = 1$, etc.

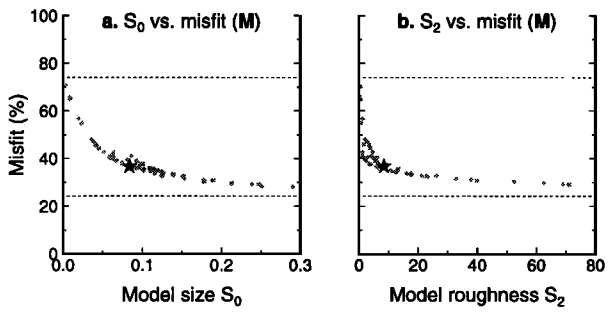

Figure 4. The misfit versus (a) the size (S_0) and (b) roughness (S_2) of models inverted using damping parameters L_0 = 0, 5, 10, 15, and 20 and β = 0.001, 1, 3, 5, 10, 20, 30, 100, 300, and 1000. Bottom dashed line shows misfit for models with no damping, and top dashed line shows misfit with the mantle corrections but no lower layer. The star shows our preferred model ($L_0 = 15, \beta = 10$).

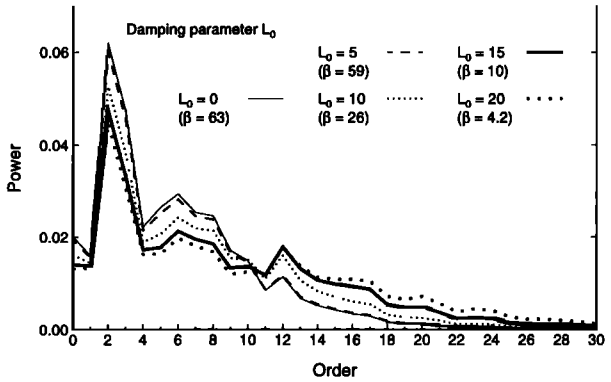

Figure 5. The power in each order for L_0 = 0, 5, 10, 15, and 20. Values of β are adjusted to keep the variance reduction constant at the level in our preferred model (63%).

The parameter β can be viewed as the standard trade-off parameter between data misfit and model norm. For order less than L_0 this solution seeks the smallest model, while for orders larger than L_0 the smoothest model is returned. This can be seen by looking at the structure of $\mathbf{D}$. For $l(i) \ll L_0$, $\mathbf{D}(i,i) \approx \beta \times L_0^2(L_0+1)^2$, minimizing S_0. For $l(i) \gg L_0$, $\mathbf{D}(i,i) \approx \beta \times l(i)^2(l(i)+1)^2$, minimizing S_2.

3.2. Trade-offs Between Amplitudes and Misfit

Figure 4 charts the size S_0 and roughness S_2 versus the misfit from models inverted using different values of L_0 and β. Without a basal layer the upper and middle mantle corrections from model S16B30 [*Masters et al.*, 1996] (described in section 3.4.1) explain 26% of the variance. Models inverted using the mantle corrections and no damping are unstable but explain 75% of the variance. Imposing damping by increasing either β or L_0 decreased the model size but increased the data misfit. Examining the trade-off curves of data misfit versus model size S_0 and versus model roughness S_2 (Figure 4), we chose the model with $L_0 = 15, \beta = 10$ as our preferred model. Combined with the upper and middle mantle corrections, they reduce 63% of the variance (star, Figure 4) and 62% and 64% of the variance in the *ScS-S* and S_{diff}-*SKS* travel times, respectively. Note that unless otherwise stated, the variance reductions listed in this text include the variance reduction from both the mantle corrections and the basal layer.

To look at the power present at each degree l in the models, we inverted the data with L_0 = 0, 5, 10, 15, and 20 and chose β such that the variance reduction stayed constant at 63% (Figure 5). For every model, regardless of the damping, the model power dramatically peaks at degrees l = 2 and 3 with smaller peaks at l = 6, 8, and 12. Our models were inverted to order $L_{\max}$ = 30. The effects of spectral leakage, the contamination of lower-degree wavelengths by higher-degree structures due to cutoff and aliasing effects, can be considerable, especially on the small-scale heterogeneity pattern [*Mégnin and Romanowicz*, 2000a]. To avoid aliasing from degrees greater than 30 into lower degree structures, the power should smoothly go to zero as l approaches 30. The roughness (Laplacian) damping effec-

tively accomplishes this by smoothly damping power at orders $l > L_0$. This damping can be seen in Figure 5: the power at $l = 30$ is larger for $L_0 = 20$ than for $L_0 = 0$, 5, 10, and 15.

3.3. Only S_{diff}-*SKS* and Only *ScS-S*

We also inverted the *ScS-S* and S_{diff}-*SKS* data sets independently using mantle corrections from model S16B30 [*Masters et al.*, 1996] (Figure 6). The resulting models explain 63% and and 66%, respectively, of the variance in their data subset and 49% and 56%, respectively, of the variance in the complete data set. Obvious differences exist in regions where the sampling is not even (see Figure 2). For example, the *ScS-S* sampling is relatively poor underneath the central Pacific and between Madagascar and Antarctica, while the S_{diff}-*SKS* sampling is relatively poor beneath southern South America.

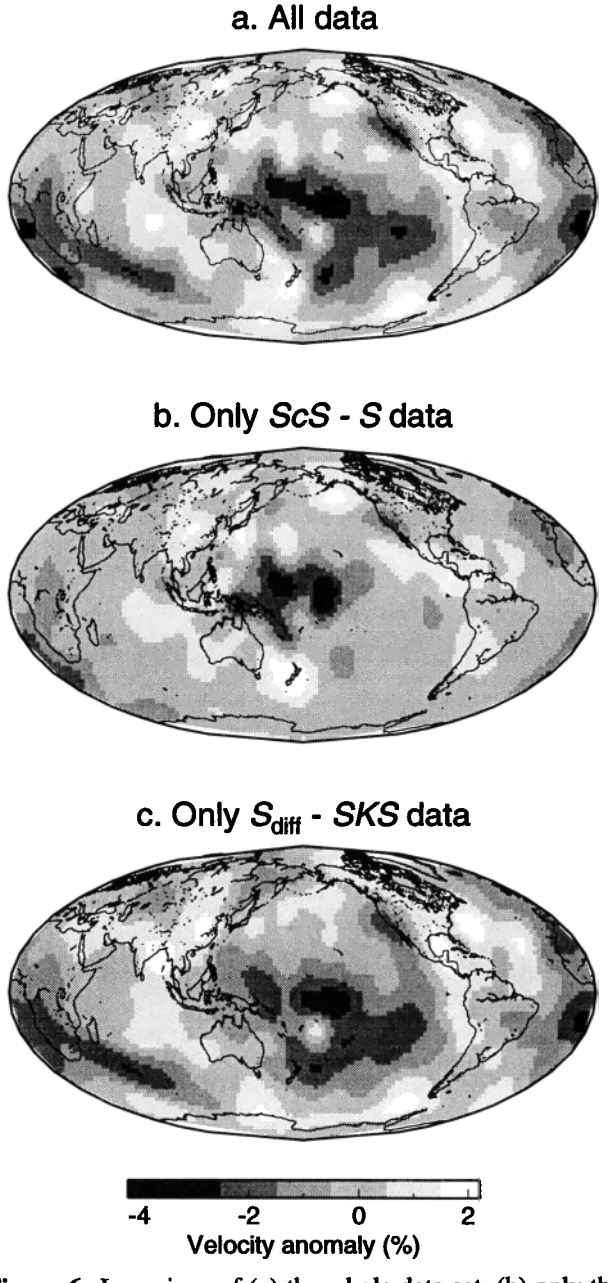

Figure 6. Inversions of (a) the whole data set, (b) only the *ScS-S* data set, and (c) only the S_{diff}-*SKS* data.

3.4. Three-Dimensional Mantle Corrections

Mantle structures outside of the basal layer contribute to the differential travel times; we must account for them to prevent projecting shallower mantle structure into the basal wave speed model. Obviously, differences between 3-D mantle models change these contributions and thus our resulting model. The differential residual time method attempts to mitigate errors in mantle models by using phases with similar ray paths such that unmapped anomalies outside of the basal layer will similarly affect both rays. As the ray paths diverge, unmapped anomalies affect the phases independently. While 3-D S_{diff}-*SKS* sensitivity kernels of the residual times show nontrivial sensitivity at midmantle depths, the sensitivity peaks in the bottom 250 km of the mantle (H. Kárason and R. D. van der Hilst, Improving the tomographic imaging of the lowermost mantle by incorporation of differential times of refracted and diffracted core phases (*PKP*, P_{diff}), submitted to Journal of Geophysical Research, 2000). Along with the long paths across the base of the mantle, especially for the S_{diff} phase, these observations argue that the travel times that we inverted are most sensitive to structure at the base of the mantle and less sensitive to shallower structures.

3.4.1. Whole mantle 3-D model corrections. To calculate the contribution of a given 3-D velocity model, we first traced rays through the PREM model, calculating the latitude, longitude, and travel time at points spaced evenly at 10 km depths along the ray. The first-order contribution to the travel time from the mantle model is estimated by

$$\Delta t^{\text{model}} = -\int_{\text{path}} \frac{\delta v}{V^2} dl = -\int_{\text{path}} \frac{\delta v}{V} dt, \qquad (9)$$

where δv is the velocity perturbation from the 3-D model, V is the velocity from the PREM model at the corresponding depth, dl is the path length increment, dt is the travel time increment, and path is the ray path outside of the basal layer.

For each of six 3-D mantle models we calculated corrections for our differential travel time observations and inverted the "corrected" differential residuals times for basal layer structure using $\beta = 10, L_0 = 15$. The models included four models derived using spherical harmonics: models S16B30 [*Masters et al.*, 1996], S12_WM13 [*Su and Dziewonski*, 1991], S16U6L8 [*Liu and Dziewonski*, 1998], and SAW24B16 [*Mégnin and Romanowicz*, 2000b] and two models derived using blocks, the 1997 model of *Grand et al.* [1997] and the 1998 model of *Widiyantoro et al.* [1998]. Figure 7 illustrates the corrections from each of the six models. Differences exist both in amplitude and in the distribution of the resulting anomalies, possibly due to differences in data and damping between 3-D models. For example, the Widiyantoro model, which was developed using a heavily culled *S* wave data set [*Engdahl et al.*, 1998], has relatively small amplitudes in the midmantle and without a basal layer

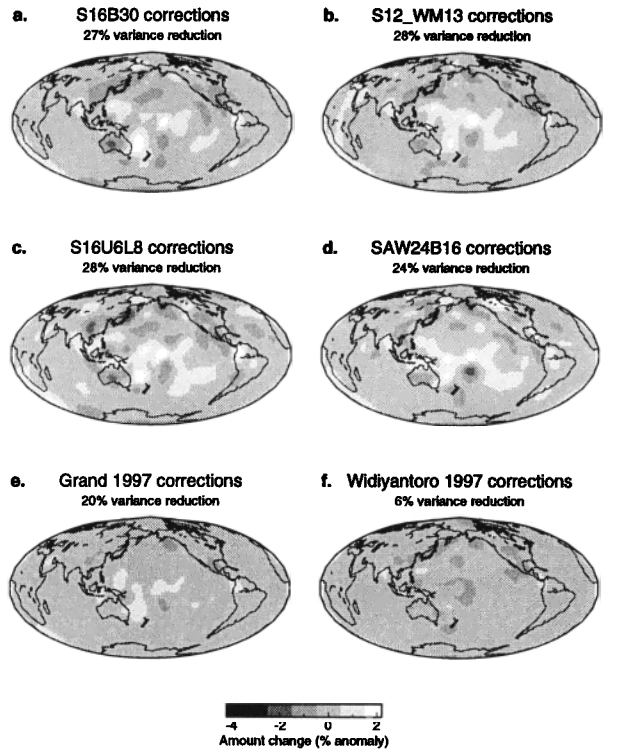

Figure 7. Corrections for nonbasal layer 3-D mantle structures. Each plot shows the difference between the basal wave speed model determined with and without the listed mantle corrections. The variance reduction listed shows how well the nonbasal structures (above 2600 km depth) in each model satisfy our travel times.

explains only 6% of the travel time variance. Conversely, model S16B30 has larger amplitudes in the midmantle; this model explains 26% of the variance without a basal layer.

While there are differences, the corrections are remarkably robust. Optimistically, the stability suggests that the mantle models do a good job of representing the large-scale structure of the mantle. Pessimistically, one might argue that the mantle models have converged on an inaccurate model of the Earth; for example, congruence of mantle models in the Southern Hemisphere south of 45°S may be due to a paucity of sampling. While small-scale midmantle structures underrepresented in these 3-D models might be mapped into our model, the long wavelengths of the *ScS*, *S*, S_{diff}, and *SKS* waves dissipate their effect. Furthermore, without the mantle corrections our model would have larger absolute anomalies: the mantle corrections actually decrease the absolute anomaly under the mid-Pacific by several percent. The features of the model that we interpret, such as correlations with hotspot locations and subduction zones, are robust and equally strong regardless of the corrections used.

3.4.2. Travel time anomalies from slabs. Cold and therefore seismically fast slabs decrease the travel time of any ray traveling through them. Because of the limited resolution and tendency to spatially average narrow velocity anomalies, global *S* velocity models generally do not accurately image narrow upper mantle slab structures. For earthquakes within cold slabs, fast slab anomalies contribute disproportionately to phases with different takeoff angles, especially to *ScS-S* times recorded at short epicentral distances.

To investigate the slab influence on *ScS-S* travel times, we defined a surface representing the slab center using seismicity [*Gudmundsson and Sambridge*, 1998]. We modeled the slab velocity anomaly as a Gaussian distributed anomaly with a 5% fast center which falls to 2.5% fast at 75 km from the center. We applied equation (9) to calculate travel time corrections for *ScS* and *S*. For depths <250 km, earthquakes appear to occur at the top of the slab rather than in the middle [*Engdahl and Gubbins*, 1987]; defining the slab as surrounding the seismicity thus introduced a minor error. Furthermore, this only corrects for the seismically active portion of the slab and not for aseismic extensions of the slab.

Owing to slab geometries, this correction is generally very small. One place where it may be important is for direct and depth phases from Tonga-Fiji earthquakes to stations TAU and NWAO in Australia. Nevertheless, the mean and standard deviation of this correction, -0.25 s (faster) and 0.89 s, were small compared to a standard deviation of 3.13 s for travel time residuals from the *ScS-S* data set. The rms of the velocities in the model including these slab corrections was 1.41 km s^{-1}; without these corrections the rms was 1.40 km s^{-1}. We conclude that these corrections are insignificant except in special locations and have therefore decided to not incorporate them.

3.5. Anisotropy

3.5.1. Anisotropy in the upper mantle. All of the waves are horizontally polarized shear waves (*SH* waves) except for *SKS*, which is a vertically polarized shear wave (*SV*). Therefore upper mantle anisotropy could introduce travel time anomalies. Anisotropy measurements exist under approximately half of stations recording S_{diff}-*SKS* times [*Silver and Chan*, 1991]; we corrected the residuals for this anisotropy using methods described by *Kuo and Wu* [1997]. The mean and standard deviation of this correction were 0.04 s (slow) and 0.78 s, compared to a standard deviation of 4.89 s for the overall observed S_{diff}-*SKS* residuals.

When we inverted only the S_{diff}-*SKS* times, the splitting corrections changed the extrema by <0.1% and the model rms by <0.01%: qualitatively insignificant. For stations for which no anisotropy corrections exist, we did not add corrections. We feel the small size of the correction justifies this omission.

3.5.2. Anisotropy at the base of the mantle. In the basal layer the *SH* particle motion of *ScS* and S_{diff} is horizontal. Similarly, the *SKS* ray angle is steep so that its wave motion is also nearly horizontal. Therefore "radial anisotropy," inferred to exist near the base of the mantle [*Kendall and Silver*, 1996], most likely plays a minor role in the observed travel times. On the other hand, azimuthal anisotropy near the base of the mantle could have a large effect on effect on either *ScS-S* or S_{diff}-*SKS* travel time variations [e.g., *Preston et al.*, 1998]. Large-scale regions such as the southwest Pacific have enough crossing paths to verify that this region is indeed very slow, although an azimuthal anisotropy signal

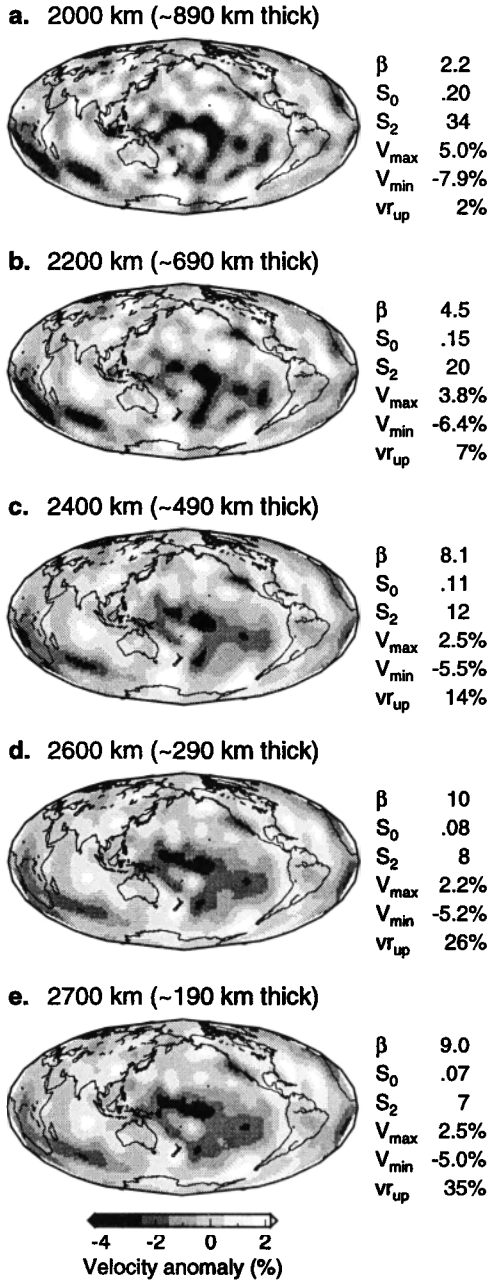

Figure 8. Models with different layer thicknesses. The velocity in the layer is vertically constant. We chose β such that the total variance reduction in each model is 63%. The size S_0 and roughness S_2 of each model have been scaled (see text); vr_{up} is the amount of variance reduction from the overlying mantle.

may be superimposed on this. We did not attempt to invert for anisotropy.

3.6. Vertical Resolution

We first assumed that the basal layer begins at 2600 km depth and inverted for velocities in the bottom 290 km of the mantle. To test the sensitivity of these data to layer thickness, we inverted the travel times using 190-, 290-, 490-, 690-, and 890-km-thick layers. We recomputed both the 3-D model corrections for structure outside of the basal layer and the sensitivity kernels. To make a fair comparison, we fixed $L_0 = 15$ and varied β to find the model at each layer thickness that produced the same variance reduction. The models, their size S_0, and roughness S_2 are plotted in Figure 8. The resulting S_0 and S_2 have been scaled by the square root of each layer thickness relative to 290 km (equations (3) and (4)).

The sensitivity kernels are such that nearly horizontally propagating rays (e.g., S_{diff} at the base of the mantle) have no dependence on layer thickness as long as the layer thickness exceeds the first Fresnel zone, which is of order 250 km. For nearly vertical rays (e.g., *SKS* and *ScS*) the size of a velocity anomaly is inversely proportional to the assumed layer thickness. The models with assumed thicknesses of 190, 290, and 490 km are nearly indistinguishable. However, if the model is more than 490 km thick, the mantle corrections decrease rapidly, and the model size S_0 and roughness S_2 required to obtain the specified fit increase dramatically. The degree 2 structure appears similar for all thicknesses, confirming *Su et al.*'s [1994] and *Liu and Dziewonski*'s [1998] conclusion of a roughly constant degree 2 structure below 2000 km. However, because thick models that fit the data require a marked increase in small-scale structure and large extrema, we conclude that layer thicknesses exceeding 490 km can be ruled out. This test assumes no radial variation within the layer and thus does not preclude localized anomalies extending higher into the lower mantle [e.g., *Breger and Romanowicz*, 1998; *Ritsema et al.*, 1998].

As the wave speed extrema grow so large, we feel that we can seismically rule out these thicknesses as viable. The wave speed extrema remain roughly constant for model thicknesses between 190 and 290 km. As several seismic observations suggest that large gradients exist ≈260 km above the CMB [e.g., *Wysession*, 1996a], we prefer the model with a 290-km-thick layer. We cannot determine this value conclusively and thus state that the model represents some sort of vertical average of the lower few hundred kilometers of the mantle.

3.7. Sensitivity Kernels

When inverting 1-Hz travel times for D" structures with length scales >100 km, the rays can be assumed to travel along infinitely thin ray paths [*Nolet and Dahlen*, 2000]. At lower frequencies the wavefront samples a broader swath as it propagates through the mantle such that the arrival time becomes more sensitive to structures off of the infinitely narrow ray path. This frequency dependence of sensitivity kernels complicates inverting of data sets combined of travel times picked at different frequencies, such as 0.05-Hz S_{diff} and 0.5-Hz International Seismological Centre (ISC) S times. It is currently too time consuming to routinely compute exact finite volume sensitivity kernels for the phases used here [see *Zhao et al.*, 2000]; nevertheless, future whole mantle inversions will benefit by incorporating finite frequency sensitivity kernels.

Plate 1 compares the models inverted using different sized sensitivity kernels. Figure 1b shows the model based on kernels that approximate the size of the Fresnel zone; Plate 1a

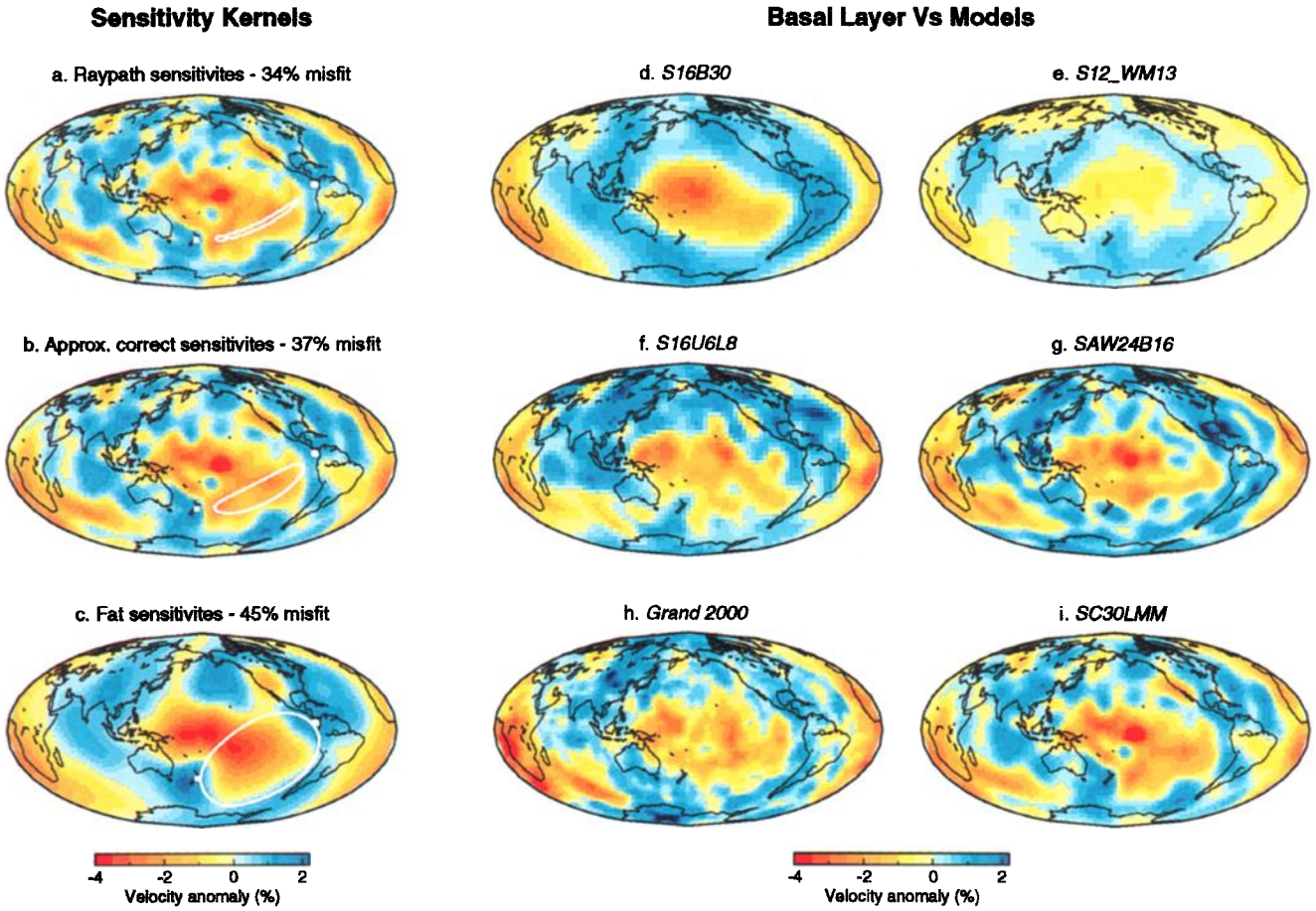

Plate 1. (left) The model after inverting using different sized sensitivity kernels. The white line contours where the sensitivity kernel for an S_{diff} arrival falls to $(2e)^{-1}$. (a) Small sensitivity kernels, similar to the infinite frequency ray paths. (b) The kernels used in this study that approximate the size of the Fresnel zone in the lowermost region. (c) Enlarged sensitivity kernels. (middle and right) V_s models of the base of the mantle: (d) S16B30, (e) S12_WM13, (f) S16U6L8, (g) SAW24B16, (h) Grand 2000, and (i) SC30LMM (Shear-Castle-degree30-lowermost mantle).

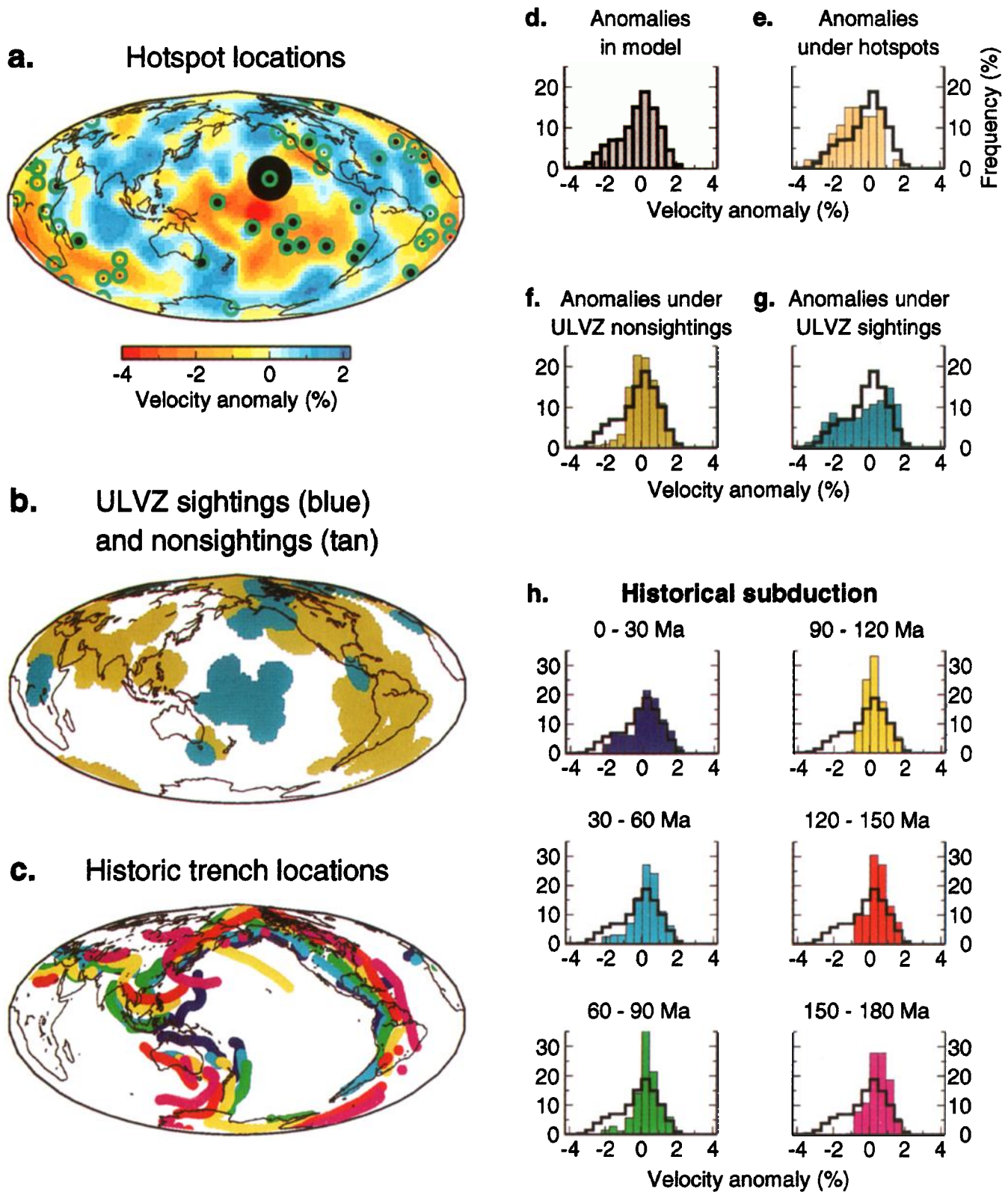

Plate 2. (a) The locations of hotspots [*Sleep*, 1992] with the velocity model SC30LLM. (b) The locations of ULVZ sightings and nonsightings [*Garnero et al.*, 1998]. (c) Historical trench locations [*Richards and Engebretson*, 1992]. Colors represent the age of the trench (see Plate 2h). (d) Histogram of velocities in the model. Solid lines in other histograms repeat this distribution. (e) The distribution of velocities under hotspots. (f and g) Velocities under ULVZ nonsightings and sightings. (h) Velocities beneath historical trench locations.

shows the results with kernels that are more similar to infinite frequency ray paths; and Plate 1c shows the model based on very large kernels. The models based on larger kernels have less small-scale structure and yield a smaller variance reduction. The differences between the models based on the infinite frequency kernels (Plate 1a) and the more realistic kernels (Plate 1b) are minor. Thus for lowermost mantle models, if the data coverage is good and the shape of the sensitivity kernel is simple, such as for S waves, the inclusion of sensitivity kernels has a secondary effect. For this reason we anticipate that the differences between using our approximate kernels and the more accurate kernels of *Zhao et al.* [2000] are minor.

3.8. Error Calculations

We made several assumptions in this inversion. First, we assumed that the velocity anomalies do not distort ray paths. The stability of the travel times to small ray path changes (i.e., Fermat's principle) and the use of wide sensitivity kernels both justify this assumption. Second, we assumed that velocities in the basal region are vertically constant, which seems plausible given the poor vertical resolution of the data considered.

Because of the limited size of the model we were able to use a bootstrap method [*Efron and Tibshirani*, 1986] to test the uncertainty of the model assuming that errors in the data are independent of one another. We omitted a randomly chosen 10% of the data, performed the inversion, repeated 99 times, and found the standard deviation at each point (Figure 9a). These error estimates account for random errors and sampling geometry but not for correlated errors, such as incomplete corrections for 3-D midmantle structures. Uncertainties in the Southern Hemisphere are greater, especially to the southeast of New Zealand and southeast of Madagascar, where data coverage is sparse (Figure 2). Figures 9b & 9c show the results of a checkerboard test which support the inference of the bootstrap calculation. We calculated travel times for the model in 9b and inverted them. The features in the Northern Hemisphere are well resolved, while resolution is poorer in the Southern Hemisphere, especially southeast of Africa and between New Zealand and South America.

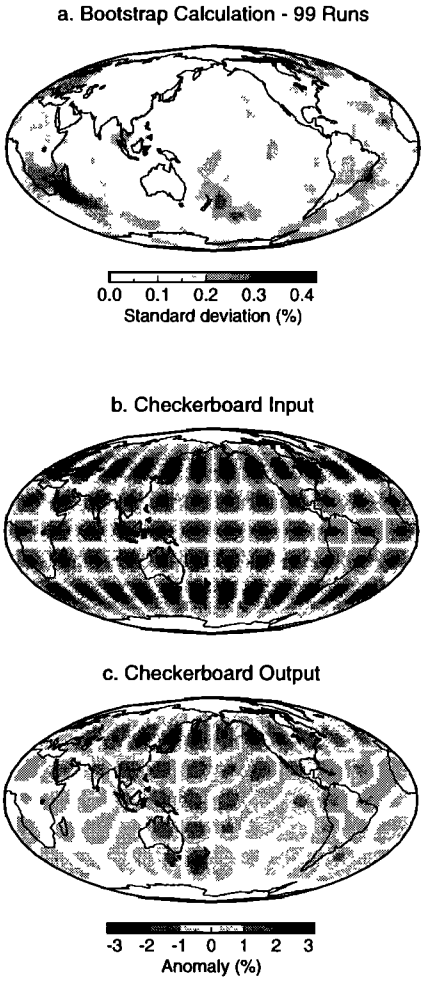

Figure 9. (a) Bootstrap error uncertainty. Shading shows the standard deviation of the 99 models at each point. (b) The spherical harmonic input model for the checkerboard test. (c) Output of the checkerboard test.

3.9. Comparison With Other Models

Several S wave mantle tomography studies have resolved the low degree structure at the base of the mantle [e.g., *Masters et al.*, 1996; *Su et al.*, 1994] (Plates 1d & 1e). Increased data have allowed more detail to be resolved, either by using higher-order spherical harmonics [e.g., *Liu and Dziewonski*, 1998; *Mégnin and Romanowicz*, 2000b] (Plates 1f & 1g) or smaller block sizes [e.g., *Grand et al.*, 1997] (Plate 1h).

In contrast, several groups have used 2-D models to investigate the lowermost mantle [e.g., *Valenzuela et al.*, 2000; Kuo et al., submitted manuscript, 2000]. While these models were inverted using independent data sets and different inversion methods, their results are similar to our model. Furthermore, by using residual travel time pairs and inverting for a 2-D basal model, these groups and ourselves were able to explore the damping parameter space, to estimate errors, to try different model parameterizations, and to investigate the effects of sensitivity kernels.

It is worthwhile to compare our 2-D model with the lowermost mantle structure deduced from whole mantle inversions. For the *ScS-S* and S_{diff}-*SKS* travel time residuals, our model explains 63% of the variance. Our variance reduction is slightly worse than that of model S16U6L8. We note that (1) the variance reduction increases when using infinite frequency ray-tubes instead of sensitivity kernels (Plate 1) and (2) the variance reduction should increase with a greater number of variables (i.e., 3-D versus 2-D). However, a direct comparison of variance reduction is neither warranted nor helpful because the number of data, the number of model parameters, and the damping methods are all different.

Remarkable agreement exists at the base of the mantle among the four recent models (Plates 1f, 1g, 1h, & 1i). Comparing SC30LLM (our model) to S16U6L8, SAW24B16, and Grand's, which all used independent data sets and different parameterizations, we observe that not only are the large-scale structures similar but many of the small-scale struc-

tures appear very similar, such as the shape of the anomalies beneath Africa and the Pacific. Differences exist in regions such as under South America and the South China Sea.

4. Interpretation and Comparisons With Other Geophysical Observations

4.1. History of Subduction

Subduction zones at the Earth's surface correlate to fast wave speeds at the base of the mantle [e.g., *Su and Dziewonski*, 1991]. Here we show that a correlation exists between the time since subduction and fast wave speeds at the base of the mantle. Plates 2c and 2h compare historical trench locations [*Engebretson et al.*, 1992] to velocity anomalies in the basal layer (Plate 2d). The dark solid line in the histograms shows the distribution of velocities in the model. Similar to other models of the lowermost mantle, the distribution has a large skewness, the difference between the mean and median [*Yanagisawa and Hamano*, 1999]. A randomly chosen set of model points should have a similar distribution. The distribution of basal wave speeds under the regions where subduction began during the most recent 30 Myr is similar to the global distribution. In contrast, the older subduction, especially subduction prior to 90 Ma, correlates extremely well with fast anomalies. We interpret the fast wave speeds as the cold thermal signature of slabs in the lowermost mantle. Assuming that slabs descend vertically through the upper mantle at a velocity of 5 cm yr^{-1} and that some slabs reach the lowermost mantle (2400 km depth) in less than 90 Myr (Plate 2h) implies that slabs descend as fast as 2 cm yr^{-1} through the lower mantle, i.e., slightly faster than the 1.5 cm yr^{-1} deduced by *Grand* [1994] and *van der Hilst et al.* [1997].

Only two fast anomalies exist under regions where no subduction appears in the *Engebretson et al.* [1992] model: one between Hawaii and Central America and the other south of India. Subduction of the Kula Plate during the Cretaceous took place in the middle of the Pacific. While the subduction history map shows the subduction ending just east of Hawaii, it likely continued farther to the southeast between Hawaii and Central America (D. Engebretson, personal communication, 1997). Additionally, while the Tethys Ocean closed as India moved northward from near South Africa, subduction may have occurred to the south under India in addition to subduction under Asia.

Both the basaltic and harzburgite components of subducting slabs appear to be intrinsically less dense than primitive lower mantle [*Kesson et al.*, 1998], so a slab should become positively buoyant even before it thermally equilibrates. That most slabs appear to reach the bottom of the mantle suggests that they have considerable thermal inertia. The correlation between historic trench locations and slow wave speeds continues through the subduction history from 90 to 180 Ma, suggesting that slabs remain at the bottom of the mantle for at least 90 Myr. Unfortunately, the historical record ends near 180 Ma, preventing us from determining how long slabs reside at the bottom of the mantle.

4.2. Hotspots

Slow wave speeds in the lowermost mantle from degree 2 models correlate well with hotspot locations [e.g., *Richards et al.*, 1988]. In our degree 30 model, slow regions correlate to the surface location of hotspots (Plates 2a & 2e), supporting previous observations. If no correlation existed between hotspot locations at the surface and slow anomalies in the lowermost mantle, it would strongly argue that hotspots do not originate within the basal layer. Unfortunately, the converse is not necessarily true: hotspots overlaying slow velocities implies only that hotspots may originate in the basal layer but does not require it. Nevertheless, in order to correlate hotspot locations and slow wave speeds, any layered mantle convection model in which hotspots originate at a thermal boundary layer at shallower depths [e.g., *Kellogg et al.*, 1999] must predict slow velocities at the base of mantle beneath hotspots.

As an interesting observation, many hotspots overlay the edges of slow anomalies: for examples, Hawaii sits just to the northeast of the mid-Pacific slow anomaly, eastern Pacific hotspots lie at the eastern edge of the mid-Pacific slow anomaly, hotspots in North America are at the eastern edge of a slow anomaly under western North America, and several hotspots bound the southern African/Madagascar slow anomaly. One explanation is that hotspots originate at the edges of downgoing slabs and represent a dynamic instability in which the chemically buoyant slab reaches the temperature at which it becomes buoyant and ascends.

Alternatively, hotspots may initiate at the slowest regions in the lowermost mantle and, owing to horizontal flow in the lower mantle, migrate horizontally while ascending. Indeed, the predicted latitudes and longitudes of hotspot sources at the base of the mantle [*Steinberger*, 2000] correlate extremely well with slow regions in our model. Admittedly, some circular reasoning exists as mantle tomography models are used to calculate whole mantle flow and to derive the hotspot trajectories. Also, the plume ascent rate and the ability of a plume conduit to survive shear strain without initiating a newer, more vertical, conduit depend on plume and mantle viscosities, both of which are temperature-dependent [*Zhong et al.*, 2000]. Nevertheless, 3-D spherical mantle flow models with temperature-dependent viscosity and surface plates suggest that plumes originate in the lowermost mantle away from downwellings (subduction) and can travel up to 14° horizontally (angular distance) while ascending [*Zhong et al.*, 2000].

4.3. ULVZs

Distorted waveform shapes and abnormal seismic precursors suggest the existence of localized zones of ultralow velocity (ULVZs) in the lower 5 to 50 km of the mantle [*Mori and Helmberger*, 1995; *Garnero and Helmberger*, 1996]. Extreme decreases in wave speed could be caused by regions of partial melt [*Williams and Garnero*, 1996; *Revenaugh and Meyer*, 1997], which could be the source material of mantle plumes [*Williams et al.*, 1998].

Places where ULVZs are observed to not exist rarely occur where we observe wave speeds slower than 1% (Plate 2f), suggesting that all regions that are very slow contain an ULVZ. However, ULVZ sightings do not obviously correlate with slow anomalies. ULVZs have indeed been sighted under the middle of the Pacific and under Africa, both extremely slow regions, but they have also been sighted under Alaska and Central America, both fast regions. Depending on whether ULVZs occur only in hot regions, these observations suggest either that (1) if ULVZs occur only in warm regions, the map of ULVZ locations (Plate 2b) is incorrect or (2) that ULVZs exist wherever wave speeds are very slow but are not limited to these regions. For example, our study of the CMB beneath the Gulf of Alaska using *ScP* phases [*Castle and van der Hilst*, 2000] shows that this area is not an ULVZ for shear wave speeds (not an ULVsZ). Either the ULVpZ imaged there (Plate 2b) is incorrect or the ULVZ is only for compression wave speeds. Further comparisons between velocity anomalies and ULVZs require better characterization of ULVZs, such as their thicknesses.

To check if ULVZs would affect the travel times, we computed long-period complete synthetic seismograms [*Cummins et al.*, 1994] with and without a 20-km-thick ULVZ with a 30% V_s drop, a 10% V_p drop, and 10% density increase. Comparisons between the two show that an ULVZ significantly affects *ScS* and S_{diff} travel times such that ULVZs and partial melt could explain the large slow wave speed anomalies and the non-Gaussian histogram of anomalies. While our model assumes a layer of vertically constant velocity, a thin ULVZ obviously breaks this assumption. However, it does not invalidate our results; rather, our models should be viewed as a vertical average over the lowermost mantle.

5. Thermal Anomalies?

Several ways of converting velocity anomalies to thermal anomalies exist. *Wang and Weidner* [1996] employ

$$(\partial \ln V_s/\partial T)_P = 1/2[(\partial \ln \mu/\partial T)_P + \alpha], \qquad (10)$$

where μ is the shear modulus, α is the thermal expansivity, and P is the pressure. Along with $|\partial\mu/\partial T| = 0.024$ GPa and α values from their previous work, they find $\delta T = -2.6 \times 10^4 \delta V/V$ at the CMB.

The extreme velocity anomaly values in our inversion are 2.2% fast to 5.2% slow (mean = -0.20%, median = 0.005%). Eliminating the most extreme values, which cover only 0.3% of the area of the basal layer, the extrema would range from 2.2% fast to 4.0% slow, consistent with extrema from other mantle models which typically range from 3% fast to 4% slow. Assuming purely thermal anomalies would require temperature variations of -575°K (cold) to +1050°K (hot).

Geodynamical modeling of plume initiation suggests that if thermal anomalies of 800°K exist at the CMB in an unlayered, homogeneous lower mantle, plumes would nucleate and arrive at the Earth's surface with an excess temperature of over 480°K, much greater than the observed 300°K excess plume temperature [*Farnetani*, 1997]. Therefore the observed velocity anomalies appear too large to be attributed solely to thermal anomalies. Explanations of the large wave speed extrema other than solely thermal variations include (1) large regions of material softening or partial melt in the hottest (slowest) regions, which would dramatically increase anelastic wave speed contributions [*Karato*, 1993], and (2) widespread compositional anomalies.

If a warm lower layer exists, such as a layer of partial melt (e.g., a ULVZ), models of thermal boundary layers in the lower mantle illustrate that it will be entrained into mantle convection unless it is stabilized by compositional density increases [*Sleep*, 1988; *Farnetani*, 1997]. Thus compositional changes, such as an enrichment in iron or silicon in the lower portion of the lower mantle, would stabilize this region. An iron enrichment in regions away from downwellings could explain the anomalously slow wave speeds. These regions, slow both from excess temperature and increased iron content, would nevertheless be stable due to increased density from the iron [*van der Hilst and Kárason*, 1999].

6. Conclusion

We used 1671 S_{diff}-*SKS* and 4864 *ScS*-*S* travel time residuals to invert for shear wave velocity anomalies at the bottom of Earth's mantle. We attempted to correct for all sources of travel time residuals outside of the basal layer. The fast velocities in the resulting model correlate well with older subduction, implying that slabs reach the bottom of the mantle in ≈90 Myr and reside there for at least another 90 Myr. Hotspots correlate well with slow anomalies, consistent with the hypothesis that they originate in the lowermost mantle, while correlations with ULVZs suggest that ULVZs exist both under slow wave speed regions and under some fast regions. The anomalies range from 2.2% fast to 5.2% slow. Using thermal/velocity scaling relationships, these anomalies are too large to be explained solely thermally; rather, there must exist alternative explanations such as partial melt or composition variations at the base of the mantle. Iron enrichment in the slow regions is an attractive candidate.

Acknowledgments. We thank E. Garnero, B. Kuo, G. Masters, and M. Wysession for generous access to travel time data sets; J. M. Brown, E. Garnero, R. Merrill, L. Preston, and M. Wysession for helpful discussions; S. Grand, C. Mégnin, and S. Widiyantoro for unpublished tomography models; and E. Garnero for a review. Figures were created with GMT [*Wessel and Smith*, 1995]. Most of the seismograms that we analyzed were recorded and distributed by the Incorporated Research Institutions for Seismology and Geoscope. This research was supported by the National Science Foundation (EAR9814614).

References

Bloxham, J., and D. Gubbins, Thermal core-mantle interactions, *Nature*, *325*, 511–513, 1987.

Breger, L., and B. Romanowicz, Three-dimensional structure at the base of the mantle beneath the central Pacific, *Science*, *282*, 718–720, 1998.

Buffett, B. A., Geodynamic estimates of the viscosity of the Earth's inner core, *Nature, 388*, 571–573, 1997.

Bullen, K. E., The interior of the Earth, *Sci. Am., 193 (3)*, 56–61, 1955.

Castle, J. C., and R. D. van der Hilst, The core-mantle boundary under the Gulf of Alaska: No ULVZ for shear waves, *Earth Planet. Sci. Lett., 176*, 311–321, 2000.

Cummins, P. R., R. J. Geller, and N. Takeuchi, DSM complete synthetic seismograms: *P-SV*, spherically symmetric, case, *Geophys. Res. Lett., 21*, 1663–1666, 1994.

Dziewonski, A., and D. L. Anderson, Preliminary reference Earth model, *Phys. Earth Planet. Inter., 25*, 297–356, 1981.

Dziewonski, A. M., and F. Gilbert, The effect of small, aspherical perturbations on travel times and re-examination of the corrections for ellipticity, *Geophys. J. R. Astron. Soc., 44*, 7–18, 1976.

Efron, B., and R. Tibshirani, Bootstrap methods for standard errors, confidence intervals, and other measures of statistical accuracy, *Stat. Sci., 1*, 54–77, 1986.

Engdahl, E. R., and D. Gubbins, Simultaneous travel time inversion for earthquake location and subduction zone structure in the central Aleutian Islands, *J. Geophys. Res., 92*, 13,855–13,862, 1987.

Engdahl, E. R., R. D. van der Hilst, and R. P. Buland, Global teleseismic earthquake relocation with improved travel times and procedures for depth determination, *Bull. Seismol. Soc. Am., 88*, 722–743, 1998.

Engebretson, D. C., K. Kelley, H. Cashman, and M. A. Richards, 180 million years of subduction, *GSA Today, 2*, 93–100, 1992.

Farnetani, C. G., Excess temperature of mantle plumes: The role of chemical statification across D", *Geophys. Res. Lett., 24*, 1583–1586, 1997.

Garnero, E. J., and D. V. Helmberger, Travel times of S and SKS: Implications for three-dimensional lower mantle structure beneath the central Pacific, *J. Geophys. Res., 98*, 8225–8241, 1993.

Garnero, E. J., and D. V. Helmberger, Seismic detection of a thin laterally varying boundary layer at the base of the mantle beneath the central-Pacific, *Geophys. Res. Lett., 23*, 977–980, 1996.

Garnero, E. J., J. Revenaugh, Q. Williams, T. Lay, and L. H. Kellogg, Ultralow velocity zone at the core-mantle boundary, in *The Core-Mantle Boundary Region, Geodyn. Ser.*, vol. 28, edited by M. Gurnis et al., pp. 319–334, AGU, Washington, D. C., 1998.

Grand, S. P., Mantle shear structure beneath the Americas and surrounding oceans, *J. Geophys. Res., 99*, 11,591–11,621, 1994.

Grand, S. P., R. D. van der Hilst, and S. Widiyantoro, Global seismic tomography: A snapshot of convection in the Earth, *GSA Today, 7*, 1–7, 1997.

Gudmundsson, O., and M. Sambridge, A regionalized upper mantle (RUM) seismic model, *J. Geophys. Res., 103*, 7121–7136, 1998.

Karato, S., Importance of anelasticity in the interpretation of seismic tomography, *Geophys. Res. Lett., 20*, 1623–1626, 1993.

Kellogg, L. H., B. H. Hager, and R. D. van der Hilst, Compositional stratification in the deep mantle, *Science, 283*, 1881–1884, 1999.

Kendall, J. M., and P. G. Silver, Constraints from seismic anisotropy on the nature of the lowermost mantle, *Nature, 381*, 409–412, 1996.

Kennett, B. L. N., E. R. Engdahl, and R. Buland, Constraints on seismic velocities in the Earth from traveltimes, *Geophys. J. Int., 122*, 108–124, 1995.

Kesson, S. E., J. D. F. Gerald, and J. M. Shelly, Mineralogy and dynamics of a pyrolite lower mantle, *Nature, 393*, 252–255, 1998.

Kuo, B. Y., and K. Y. Wu, Global shear velocity heterogeneities in the D" layer: Inversion from $Sd-SKS$ differential travel times, *J. Geophys. Res., 102*, 11,775–11,788, 1997.

Liu, L. G., Phase transformations and the constitution of the deep mantle, in *The Earth: Its Origin, Structure and Evolution*, edited by M. McElhinny, pp. 177–198, Academic, San Diego, Calif., 1979.

Liu, X.-F., and A. M. Dziewonski, Global analysis of shear wave velocity anomalies in the lower-most mantle, in *The Core-Mantle Boundary Region, Geodyn. Ser.*, vol. 28, edited by M. Gurnis et al., pp. 21–36, AGU, Washington, D. C., 1998.

Masters, G. H., S. Johnson, G. Laske, and H. Bolton, A shear-velocity model of the mantle, *Philos. Trans. R. Soc. London, Ser. A, 354*, 1385–1411, 1996.

Mégnin, C., and B. Romanowicz, A comparison between tomographic and geodynamic models of the Earth's mantle, in *History and Dynamics of Plate Motions*, AGU, Washington, D.C., in press, 2000a.

Mégnin, C., and B. Romanowicz, The 3D shear velocity structure of the mantle from the inversion of body, surface, and higher mode waveforms, *Geophys. J. Int.*, in press, 2000b.

Merrill, R. T., M. W. McElhinny, and P. L. M. Fadden, *The Magenetic Field of the Earth*, Academic, San Diego, Calif., 1998.

Mori, J., and D. V. Helmberger, Localized boundary layer below the mid-Pacific velocity anomaly identified from a PcP precursor, *J. Geophys. Res., 100*, 20,359–20,365, 1995.

Neele, F., H. de Regt, and J. VanDecar, Gross errors in upper-mantle discontinuity topography from underside reflection data, *Geophys. J. Int., 129*, 194–204, 1997.

Nolet, G., and F. A. Dahlen, Wave front healing and the evolution of seismic delay times, *J. Geophys. Res.*, in press, 2000.

Parker, R. L., *Geophysical Inverse Theory*, Princeton Univ. Press, Princeton, N. J., 1994.

Preston, L. A., K. C. Creager, and J. P. Winchester, Azimuthal anisotropy at the base of the mantle (abstract), *Eos Trans. AGU, 77* (46), Fall Meet. Suppl., F608, 1998.

Revenaugh, J., and R. Meyer, Seismic evidence of partial melt within a possibly ubiquitous low-velocity layer at the base of the mantle, *Science, 277*, 670–673, 1997.

Richards, M. A., and D. Engebretson, Large-scale mantle convection and the history of subduction, *Nature, 355*, 437–440, 1992.

Richards, M. A., B. H. Hager, and N. H. Sleep, Dynamically supported geoid highs over hotspots: Observation and theory, *J. Geophys. Res., 93*, 7690–7708, 1988.

Ritsema, J., S. Ni, D. V. Helmberger, and H. Crotwell, Anomalous shear velocity reductions and gradients in the lower mantle beneath Africa, *Geophys. Res. Lett., 25*, 4245–4248, 1998.

Silver, P. G., and W. W. Chan, Shear wave splitting and subcontinental mantle deformation, *J. Geophys. Res., 96*, 16,429–16,454, 1991.

Sleep, N. H., Gradual entrainment of a chemical layer at the base of the mantle by overlying convection, *Geophys. J., 95*, 437–447, 1988.

Sleep, N. H., Time dependence of mantle plumes: Some simple theory, *J. Geophys. Res., 97*, 20,007–20,019, 1992.

Steinberger, B., Plumes in a convecting mantle: Models and observations for individual hotspots, *J. Geophys. Res., 105*, 11,127–11,152, 2000.

Su, W. J., and A. M. Dziewonski, Predominance of long-wavelength heterogeneity in the mantle, *Nature, 352*, 121–126, 1991.

Su, W. J., R. L. Woodward, and A. M. Dziewonski, Degree 12 model of shear velocity heterogeneity in the mantle, *J. Geophys. Res., 99*, 6945–6980, 1994.

Sylvander, M., and A. Souriau, Mapping S-velocity heterogeneities in the D" region, from $SmKS$ differential travel times, *Phys. Earth Planet. Inter., 94*, 1–21, 1996.

Valenzuela, R. W., and M. E. Wysession, Illuminating the base of the mantle with diffracted waves, in *The Core-Mantle Boundary Region, Geodynam. Ser.*, vol. 28, edited by M. Gurnis et al., pp. 57–71, AGU, Washington, D. C., 1998.

Valenzuela, R. W., M. E. Wysession, and M. O. Neustadt, Lateral variations at the base of the mantle from profiles, *J. Geophys. Res., 105*, 6201–6220, 2000.

van der Hilst, R. D., and H. Kárason, Compositional heterogeneity in the bottom 1000 km of the Earth's mantle: Toward a hybrid convection model, *Science, 283*, 1885–1888, 1999.

van der Hilst, R. D., S. Widiyantoro, and E. R. Engdahl, Evidence

for deep mantle circulation from global tomography, *Nature*, *386*, 578–584, 1997.

Wang, Y., and D. J. Weidner, $(\partial\mu/\partial T)_P$ of the lower mantle, *Pure Appl. Geophys.*, *146*, 533–549, 1996.

Wessel, P., and W. H. F. Smith, New version of the Generic Mapping Tools released, *Eos Trans. AGU*, *76*, 329, 1995.

Widiyantoro, S., B. L. N. Kennett, and R. D. van der Hilst, Extending shear-wave tomography for the lower mantle using S and SKS arrival-time data, *Earth Planets Space*, *50*, 999–1012, 1998.

Williams, Q., and E. J. Garnero, Seismic evidence for partial melt at the base of Earth's mantle, *Science*, *273*, 1528–1530, 1996.

Williams, Q., J. Revenaugh, and E. J. Garnero, A correlation between ultra-low basal velocities in the mantle and hot spots, *Science*, *281*, 546–549, 1998.

Winchester, J. P., and K. C. Creager, High-resolution map of D" shear-wave velocity anomalies (abstract), *Eos Trans. AGU*, *77* (46), Fall Meet. Suppl., F459, 1997.

Woodward, R. L., and G. Masters, Lower-mantle structure from $ScS - S$ differential travel times, *Nature*, *352*, 231–233, 1991.

Wysession, M. E., Imaging cold rock at the base of the mantle: The sometimes fate of slabs?, in *Subduction: Top to Bottom, Geophys. Monogr. Ser.*, vol. 96, edited by G. E. Bedout et al., pp. 369–384, AGU, Washington, D. C., 1996a.

Wysession, M. E., Large-scale structure at the core-mantle boundary from diffracted waves, *Nature*, *382*, 244–248, 1996b.

Wysession, M. E., L. Bartkó, and J. B. Wilson, Mapping the lowermost mantle using core-reflected shear waves, *J. Geophys. Res.*, *99*, 13,667–13,684, 1994.

Wysession, M. E., T. Lay, J. Revenaugh, Q. Williams, E. J. Garnero, R. Jeanloz, and L. H. Kellogg, The D" discontinuity and its implications, in *The Core-Mantle Boundary Region, Geodynam. Ser.*, vol. 28, edited by M. Gurnis et al., pp. 273–297, AGU, Washington, D. C., 1998.

Yanagisawa, T., and Y. Hamano, "Skewness" of S-wave velocity in the mantle, *Geophys. Res. Lett.*, *26*, 791–794, 1999.

Young, C. J., and T. Lay, Multiple phase analysis of the shear velocity structure in the D" region beneath Alaska, *J. Geophys. Res.*, *95*, 17,385–17,402, 1990.

Zhao, L., T. H. Jordan, and C. H. Chapman, Three-dimensional Fréchet differential kernels for seismic delay times, *Geophys. J. Int.*, *141*, 558–576, 2000.

Zhong, S., , M. T. Zuber, L. Moresi, and M. Gurnis, Role of temperature-dependent viscosity and surface plates in spherical shell models of mantle convection, *J. Geophys. Res.*, *105*, 11,063–11,082, 2000.

J. C. Castle and R. D. van der Hilst, Department of Earth, Atmospheric and Planetary Sciences, MIT, Bldg. 54-511, Cambridge, MA 02139. (castle@quake.mit.edu)

K. C. Creager and J. P. Winchester, Geophysics Program, University of Washington, Geophysics Box 351650, Seattle, WA 98195-1650. (kcc@geophys.washington.edu)

(Received August 12, 1999; revised May 17, 2000;
accepted May 25, 2000.)